Influence of nodular structures on fracture development in fine-grained rocks: numerical simulations based on the discrete element method

Qingfeng Meng[1]

School of Earth and Environmental Sciences, University of Manchester, Manchester M13 9PL, UK

Abstract

Discrete element experiments were performed to simulate fracturing processes in nodule-bearing, fine-grained rocks. Two models that contain a collection of bonded circular particles were subjected to uniaxial compression to yield shortening and fracturing of the particle assembly. Model I with soft nodules produced incremental amount of microfractures within nodules during the early stage of deformation, followed by the generation of macro sized fractures between neighbouring nodules by microfracture coalescence. The nodule-linking fractures constituted through-going fractures that cross-cut nodules. Model II with stiff nodules produced two conjugate sets of fractures that are predominantly localized within the rock matrix. The fractures cross-cut nodule-rock interfaces and broke contact bonds of nodule surfaces and their enclosing rocks, creating opening voids between them. The nodules, as mechanical heterogeneities, responded mechanically differently to the remote stress from the rock matrix. The distorted local stress field induced by the nodules can explain the varied levels of fracture development in nodules from the rock matrix. This study demonstrates the significant impact of nodular structures on the local stress field and fracture development within nodular horizons, which is believed to be instructive for

[1] Email Address: meng.qingfeng@hotmail.com

fracture analysis in nodule-bearing fine-grained rocks that constitute caprocks, reservoir or source rocks for hydrocarbons.

Key words: nodule; fracture; fine-grained; shale; chalk; discrete element

1. Introduction

Nodular structures occur as regular to irregular, spherical to ellipsoidal discrete masses, ranging from several centimeters to up to three meters in diameter (Tucker, 2009). In general, nodules lack internal structures except for the preserved remnants of original bedding or fossils (Marshall and Pirrie, 2013). Nodules have a contrasting composition to their host fine-grained rocks, and the nodule-forming minerals typically include calcite, chert, gypsum (anhydrite), apatite and pyrite (Boggs Jr and Boggs, 2009). Nodules tend to follow specific horizons, and they grew by cementation of the hosts during early to late burial diagenesis (e.g. Irwin et al., 1977; Marshall, 1982; Raiswell and Fisher, 2000). Nodules are, thereby, considered to be have a diagenetic origin and can aid in environmental reconstructions and sequence stratigraphic interpretations of basin history (Potter et al., 2005).

Extensive studies have been focused on petrographic observations and stable isotopes of nodules, which can yield information of microbial processes, diagenetic fluids and material sources (e.g. Coleman and Raiswell, 1981; Kiriakoulakis et al., 2000; Lash and Blood, 2004; Mozley and Burns, 1993; Mozley and Wersin, 1992; Raiswell and Fisher, 2000). However, the influence of nodular structures on the local stress field and fracture development in fine-grained rocks, which are critical for fluid flow in the low-permeability systems, are not well understood. A pioneering study by Spence and Finch (2014) made investigations into the influence of nodular chert rhythmites on fracture development in chalk through discrete element modelling, and correlated fracture intensity to the mechanical properties of their host rock and chert nodules, aiding in fracture prediction in the subsurface. Nevertheless, a further quantitative study is needed to examine the role of nodules as mechanical contrasts to their host rocks in fracturing.

This paper reports a numerical modelling study of the control of nodules, either soft or stiff, on fracture development in fine-grained rocks. This paper first introduces the research method, and then shows the modelling results, followed by comparing the results to natural examples and discussing the implications of the modelling results for fracture analysis. The aims of this study are (1) to simulate sequential fracture generation, propagation and coalescence; (2) to examine fracture spatial distribution and the local stress fields distorted by nodules; and (3) to provide realistic fracture network models that are compatible with natural examples, and to enhance our understanding of the mechanical influence of nodules in fine-grained rocks. It is believed that the results presented can be instructive for fracture analysis in nodule-bearing, fine-grained rocks that serve as caprocks, reservoir or source rocks for hydrocarbons.

2. Modelling approach

2.1. The discrete element method

The discrete element method, based on the fundamental physics of Hertzian elastic, frictional particles, was first introduced by Cundall and Strack (1979) to study the behavior and interaction of granular materials. The modelled material is composed of a collection of small particles that displace independently from one another, and interact only at contacts of particles. Individual particles are governed by linear-elastic springs in compression that resists particle overlap, and contact bonding that resists both shear and tensional displacements. Once either the shear or normal bond strength is exceeded, the bond breaks and the particle interactions are governed by Coulomb frictional sliding that resists shear motion. Deformation of the bonded aggregate is driven by the movement of elastic, frictional walls and/ or gravity. The mechanical behavior of such a system is represented by the movement of each particle and inter-particle forces acting on particle contacts, which obey Newton's law of motion.

The discrete element method has been extensively used for addressing problems in structural geology across a wide range of scales, such as the modelling of normal/ reverse faults (Saltzer, 1992; Strayer and Suppe, 2002; Yamada and Matsuoka, 2005; Abe et al., 2011; Smart et al., 2011; Hardy, 2011, 2013; Schöpfer et al., 2006, 2007, 2016, 2017; Finch and Gawthorpe, 2017), strike-slip fault (Liu and Konietzky, 2018), relay structures (Imber et al., 2004), fault gauge (Abe and Mair, 2005, 2009; Guo and Morgan, 2006, 2007), detachment fold (Hardy and Finch, 2005; Vidal-Royo et al., 2011), fault-related fold (Finch et al., 2003, 2004; Cardozo et al., 2005; Hardy and Finch, 2006, 2007; Benesh et al., 2007; Hughes et al., 2014), fold and thrust belt (Burbidge and Braun, 2002; Naylor et al., 2005; Hardy et al., 2009; Dean et al., 2013; Morgan, 2015; Morgan and Bangs, 2017), and salt tectonics (Pichel et al., 2017). In particular, the discrete element models can produce realistic fractures with a finite displacement due to the particle-based nature (Schöpfer et al., 2011; Virgo et al., 2013, 2014, 2016; Spence and Finch, 2014), and provide a promising tool for fracture modelling and prediction.

2.2. Model design and setup

A two-dimensional planar model was built, which consists of densely packed particles (Fig. 1). The model is 8 m long and 4 meter wide. The model contains six equally-sized nodules with a radius of 0.4 m, each consisting of 1,189 particles (Table 1). The nodules are uniformly distributed within the rock matrix, with a spacing of 2.5 m along the x-axis and 1.7 m along the y-axis. The rock matrix consist of 68,433 particles. The particles radii range from 0.01 to 0.012 meter, following a uniform distribution. The particle density is 2600 kg/m^3.

For the rock matrix, the particle normal stiffness is 1e8 N/m, and the shear stiffness is 5e7 N/m (Table 1). The particles in the rock matrix were assigned with a value of 1e8 N/m and 5e7 N/m for the normal and shear bond stiffness, and bond cohesion and tensile strength of 5e4 N and 2e5 N respectively. For soft nodules, the values of particle stiffness and bond strength are one magnitude lower than the matrix. For stiff nodules, those values are one magnitude higher than the matrix. A friction coefficient of 0.25 was assigned to all particles. Two walls, aligned along the y-axis, define the boundaries of model. Both walls were advanced inwards at a controlled velocity to displace the particles and to induce deformation of the particle assembly. The model margins along the x-axis were free.

Broken bonds, i.e. microfractures, and their number, displacement fields, and particle contract forces were recorded for structural analysis. Six snapshots of modelling results were presented that can represent the critical stages of fracture development. Notably, although the models presented do not directly simulate any specific natural prototypes, the models aim to provide a more general framework for analyzing the mechanical influence of nodular structures in fine-grained rocks.

3. Results

3.1. Model I with soft nodules

The model remained intact until timestep 25,000, when the first microfracture was generated in nodule 3, followed by two more microfractures being generated in this nodule (see Supplementary material). At timestep 44,000, the fourth microfracture was nucleated in nodule 2. Since then, more microfractures were generated only within the nodules as compression of the bulk rock continued, leading to an increasing fracture intensity. By contrast, no microfractures were generated in the rock matrix at this stage (Fig. 2). The displacement field exhibits a rectangular, low-value zone, with the outer boundaries defined by the nodules. The particles with the lowest displacement occurred in a rectangular zone between nodules 2 and 4 (Fig. 3).

Later, microfractures started to appear in the rock matrix between nodules 2 and 3, 3 and 4, and 4 and 5, which were aligned in a linear manner (Fig. 2). Following this, the coalescence of neighbouring microfractures in the rock matrix resulted in four macro scale fractures (F1 – F4) at T3 that link neighbouring nodules. F2 and F4 are sub-parallel to each other, which constituted a more persistent fracture cross-cutting nodule 2. This process was accompanied with the thinning of the low-displacement zone, with the thinnest segments located along F1 (Fig. 3).

At a later stage (T4), F5, aligned parallel to F3, was formed to link F3, resulting in a through-going fracture that cross-cuts nodule 5 (Fig. 2). A curved fracture F6 was formed to link nodules 1 and 3. The low-displacement zone was continuously narrowed to be restricted within F3 (Fig. 3).

At T5, a new fracture F7 was generated to link nodules 2 and 4. F8 that is rooted in nodule 3, propagated towards F1 (Fig. 2). The aperture of existing fractures all increased with distinguishable fracture porosity. The displacement field exhibited a clear zonation, i.e. the inner segments of nodular zones bounded by nodule-cutting fractures, have the lowest displacement (Fig. 3).

At the final stage (T6), F8 reached nodule 1 as the second bridging fracture that link nodules 1 and 3. No more macro fractures were formed (Fig. 2). The existing fractures continued to expand with increased aperture. The low-displacement zones on the left of nodule 4 are bounded by two through-going fractures, one consisting of F1 and F8, and the other consisting of F4 and F7 (Fig. 3). One the right of nodule 4, the low-displacement zone is between a through-going fracture that consists of F3 and F5, and a sub-parallel fracture that cuts nodule 6.

From T1 to T3, the stress field exhibited pronounced zonation during the compression process (Fig. 4). Local stresses in the four circular zones of nodules are much lower than that in the rock matrix. The stresses on each side of the nodules along the x-axis are also prominently dropped. Notably, the compressive stresses were predominantly concentrated within the zone nodule-free zones, and their trajectories were aligned approximately along the x-axis. Since T4, the compressive stresses have dropped significantly, however, the compressive stresses dominated the areas between neighbouring nodules. From T5 to T6, the compressive stresses were mainly localized within neighbouring nodules, with stress trajectories being aligned parallel to nodule-linking fractures that led to fracture propagation and widening.

Fig. 5 shows the generation history of microfractures in the model with soft nodules. It is demonstrated that the rate of microfracture generation increased at the early stage, and became subsequently decreased from timestep 1.7×10^5. A total of 11,003 microfractures were produced during the entire compression process.

3.2. Model II with stiff nodules

The model with stiff nodules remained intact until timestep 2.01×10^5 when the first microfracture was formed in the rock matrix between nodules 2 and 4 (see Supplementary material). This was followed by the generation of more microfractures in the rock matrix within the nodule-bounded areas from T1 to T4 (Fig. 6). Since T3, the spatial arrangement of microfractures began to exhibit a linear manner. The particles located within the six nodules exhibit the lowest displacement comparing to the outer particles during this period (Fig. 7).

Coalescence of neighbouring microfractures led to the formation of two conjugate sets of macrofractures since T4 (Fig. 6). Fractures of set 1 are represented by F1 that cut the inner margins of nodules 3 and 4. The other set of fractures intersect with those of set 1 at rock-nodule contacts. From T5, F1 reached nodule 1 and linked with F3 that cross-cut the outer margin of nodule 6. F2 of set 1 cut the margins of nodules 3 and 5. The low-displacement zone became narrowed to be between F1 and F2 (Fig. 7).

As compression continued, F1 propagated outward and reached the model boundary at T6. This led to a through-going fracture that transects the model (Fig. 6). Microfracture intensity became higher than the earlier stages, however, no more new macrofractures were generated. The newly-formed microfractures were largely located near the existing fractures, which widened macrofracture aperture. In particular, the intersected conjugate fractures caused breakage of rock-nodule bonds and produced an opening void. Notably, no microfractures were generated in nodules till the end of the simulation. Particles with the lowest displacement are located within the damage zone of F1, followed by the rock segment between F1 and F3 (Fig. 7).

From T1 to T4, the stress field exhibited pronounced zonation, with the compressive stresses concentrated between nodules parallel to the x-axis (Fig. 8). In nodule-free zones, stresses are significant lower. Since T5, the compressive stresses have dropped significantly, especially within the nodules. However, compressive stresses dominated the fractured zones between nodules, e.g. nodules 3 and 5, which are sub-parallel to the marofractures and contributed to fracture widening. At T6, the magnitude of compressive stresses continued to be dropped, and the stresses only dominated the areas of nodules 3 and 5 and their adjacent areas.

Fig. 9 shows the generation history of microfractures in the model with stiff nodules. The fracture generation exhibits a similar trend to model I with soft nodules, i.e. an increasing generation rate at the early stage, followed by a rate reduction at the final stage. A total 5947 microfractures were produced in this model during the entire simulation.

4. Discussion

4.1. Comparison to natural examples

4.1.1. Mudstone with soft nodules

Nodular gypsum has been commonly observed in evaporite deposits worldwide (Holliday, 1970) and also on Mars (Young and Chan, 2017). Gypsum nodules have been suggested as the syndepositional structures formed in the capillary and upper phreatic zones beneath sabkha surface

(Nichols, 2009). Gypsum nodules are often concentrated in certain horizons that may represent stages of basin drying (Cosgrove, 2001).

Fig.10 shows ruptured gypsum nodules in the Triassic red marls of the Bristol Channel Basin, UK. The white, reddish nodules occur as rounded, sub-rounded or elliptic discrete aggregates of gypsum that can be easily distinguished from their host rock. Notably, gypsum veins, either horizontal or vertical, are nodule-rooted and linking neighbouring nodules in the same or adjacent horizons. These veins have been suggested to form as the result of horizontal crustal compression during basin inversion in early Cenozoic (Meng et al., 2017b). The vein fillings are likely to be sourced from vein-rooted nodules (Meng et al., 2018).

The modelling results of model 1 with soft nodules largely agree to the field observations of gypsum veins and nodules, regarding fracture pattern and spatial distribution, especially the nodule-linking, opening-mode fractures (Fig. 2). Although it is possible that the formation of those fractures could be formed due to volumetric expansion of nodules when they encountered fresh waters, the local stresses developed between gypsum nodules could have contributed significantly to the generation of nodule-linking fractures as revealed in this study.

4.1.2. Shale with stiff nodules

Limestone nodules occur commonly in organic-rich shales. Such nodules have been considered to have formed during early to late diagenesis, and have derived carbonate from seawater, dissolution of fossil skeletons or bicarbonate from bacterial decomposition of organic matter (e.g. Marshall, 1982; Wolff et al., 1992; Kiriakoulakis et al., 2000; Meng et al., 2017a).

The limestone nodules form a strong mechanical contrast between the nodules and their enclosing weak shales, and are ideal comparative objects to model 2 with stiff nodules. Fig. 11a shows limestone nodules in the Lowellville Shale of the Pottsville Group of northeastern Ohio, USA. The outcrop is transected by a fault developed between two sub-rounded, gray limestone nodules. The fault plane encounters the upper surface of nodule *a* and the lower surface of nodule *b*, resulting in peeling of nodule-enclosing shales and expose of nodule surfaces.

Similarly, multiple faults occur in highly-fractured shales that contain an elliptic limestone nodule (Fig. 11b). Faults F1' encounter the upper plane of the nodule and cross-cut its frontal tapering segment. The faults observed in the Lowellville Shale are comparable with F1 in model 2 of this study (Fig. 6). These faults/ fractures occur between neighbouring nodules, and develop along nodule-rock contacts, leading to breakage of nodule-rock bonds. Moreover, the level of fracture development exhibits a high variance between stiff limestone nodules and weak shales, i.e. fractures are much more intensively developed in shales.

4.2. Implications for fracture analysis in nodule-bearing, fine-grained rocks

It is demonstrated in the modelling results that the occurrence of nodular structures with different elastic properties from the host rock can respond mechanically differently to the remote stress (Figs 4, 8). This can distort the local stress field not only within the nodules, but also in the rock matrix around the nodules. Such mechanical contrasts can lead to varied fracture pattern, distribution, propagation and intensity. This is similar to the effect of mechanical stratigraphy on fracture development in the host strata (Laubach et al., 2009).

If nodules are weaker than their host rock, fractures are predominantly localized within nodules (Fig. 2). In contrast, fractures would be preferentially developed in the host rock if nodules are stronger (Fig. 6). This agrees to a similar experimental study by Virgo et al. (2014). In their study, the researchers found that repeated fracturing would occur in a sealed pre-existing vein if the vein is weaker than its host rock, whilst a bundle of subparallel veins would be produced if the vein is stronger than the host rock.

The localization of fracture distribution, either in the nodules or the rock matrix, can be due to the elastic mismatch between nodules and their enclosing rock, which can arrest fracture propagation and result in fracture termination at nodule-rock contacts. For rocks with weak nodules, the local stresses between neighbouring nodules can result in bridging, opening-mode fractures as a result of concentration of compressive stresses that is oriented parallel to fracture directions. For rocks with stiff nodules, the bond at interfaces between nodules and enclosing rocks can be preferentially broken and influence fracture propagation directions to be deflected along the nodule-rock contacts (Fig. 6). Hence, the occurrence of nodules can cause profound mechanical heterogeneities at a stratigraphic unit.

Evaporitic mudstones are commonly regarded as an efficient type of caprocks for hydrocarbon reservoirs because of their low ultralow permeability that can prevent fluid flow (Armitage et al., 2013, 2016; Meng et al., 2018a). Natural fractures in those rocks can indicate breaches of seals and serve as hydraulic conduits for fluid migration (Meng et al., 2018b). Therefore, the studies on natural fractures are critical for seal integrity analysis. It is shown in this study that the nodular horizons could be highly fractured if the sedimentary basin has experienced tectonic compression during its evolution.

Black shales have been intensively studies during the past decade due to the boom in shale gas development (Curtis, 2002). Notably, nodular structures, mainly including limestone and pyrite nodules, have been frequently reported in many gas-bearing shales, e.g. the Barnett Shale in the Fort Worth Basin (USA) (Bowker, 2007), the Marcellus Shale in the Appalachain Basin (USA) (e.g. Hooker et al., 2017), the Vaca Muerta Shale in the Neuquén Basin (Argentina) (e.g. Rodrigues et al., 2009), the Low Lias Shale in the Wessex Basin (UK) (e.g. Kiriakoulakis et al., 2000). It has been suggested that the production of shale gas relies on the existing natural fracture network during artificial stimulation (Gale and Holder, 2010; Gale et al., 2014). Hence, the knowledge of fracture systems in the target shales is necessary for effective hydraulic fracture treatment design. Similarly, hydrocarbon production from chalk reservoirs also depends on natural fracture networks that are intimately associated with chert nodules (e.g. Corbett et al., 1987; Belayneh et al., 2007). The modelling results presented in this study show that the occurrence of horizons of stiff limestone nodules in less stiff host rocks (shale or chalk) may not favor the generation of fractures. Fractures could be less abundant in those horizons compared to nodule-free levels. Moreover, fractures tend to cross-cut nodule-rock interfaces, suggesting that fracture orientations can be highly affected by nodules. The dilatational voids created by nodule-related fractures can significantly increase the total porosity of the bulk rock.

Notably, the numerical models presented are highly simplified, and many other factors that may potentially influence fracture development in nodular horizons were not considered, such as shapes and spacing of nodules, and fluid pressure. It is suggested that future studies can consider these factors and incorporate fluid coupling in the numerical models, so as to construct more realistic models. Moreover, the timing of fracturing, i.e. the level of lithofication, should be analyzed for inferring the mechanical properties of nodules and their hosts for the input of model parameters.

5. Conclusions

(1) This study demonstrates that numerical experiments based on the discrete element method are efficient to simulate shear and tensile fracturing in nodule-bearing, fine-grained rocks.

(2) The modelling results show that fracture generation was largely localized to soft nodules in fine-grained rocks. Bridging, opening-mode fractures were preferentially formed to link neighbouring nodules.

(3) In fine-grained rocks with stiff nodules, fractures were predominantly produced in the rock matrix. Nodule-rock contacts significantly influenced the propagation and deflection of fractures.

(4) The occurrence of nodules, either soft or stiff, responded differently to the remote stress and distorted the local stress field, and thereby affected fracture nucleation, propagation, pattern and abundance.

(5) The simulation results compare well with field examples of fractures (veins) in mudrocks with soft gypsum nodules and stiff limestone nodules, suggesting that the results can be instructive for fracture analysis in nodule-bearing fine-grained rocks serving as caprocks, reservoir or source rocks.

Acknowledgements

The author’s position is funded by the Sandstone Injection Research Group (SIRG) consortium. This study is partly funded by the SEES Postdoc Research Fund.

References

Abe, S., Mair, K., 2005. Grain fracture in 3D numerical simulations of granular shear. Geophysical Research Letters 32, L05305, doi:10.1029/2004GL022123.

Abe, S., Mair, K., 2009. Effects of gouge fragment shape on fault friction: New 3D modelling results. Geophysical Research Letters 36, L23302, doi:10.1029/2009GL040684.

Abe, S., Van Gent, H., Urai, J.L., 2011. DEM simulation of normal faults in cohesive materials. Tectonophysics 512, 12-21.

Armitage, P.J., Worden, R.H., Faulkner, D.R., Aplin, A.C., Butcher, A.R., Espie, A.A., 2013. Mercia Mudstone Formation caprock to carbon capture and storage sites: petrology and petrophysical characteristics. Journal of the Geological Society 170, 119-132.

Armitage, P.J., Worden, R.H., Faulkner, D.R., Butcher, A.R., Espie, A.A., 2016. Permeability of the Mercia Mudstone: suitability as caprock to carbon capture and storage sites. Geofluids 16, 26-42.

Belayneh, M., Matthäi, S.K., Cosgrove, J.W., 2007. The implications of fracture swarms in the Chalk of SE England on the tectonic history of the basin and their impact on fluid flow in high-porosity, low-permeability rocks. Geological Society, London, Special Publications 272, 499-517.

Benesh, N.P., Plesch, A., Shaw, J.H., Frost, E.K., 2007. Investigation of growth fault bend folding using discrete element modeling: Implications for signatures of active folding above blind thrust faults. Journal of Geophysical Research: Solid Earth 112, B03S04, doi:10.1029/2006JB004466.

Boggs Jr, S., Boggs, S., 2009. Petrology of sedimentary rocks. Cambridge University Press.

Bowker, K.A., 2007. Barnett shale gas production, Fort Worth Basin: Issues and discussion. AAPG Bulletin 91, 523-533.

Burbidge, D.R., Braun, J., 2002. Numerical models of the evolution of accretionary wedges and fold-and-thrust belts using the distinct-element method. Geophysical Journal International 148, 542-561.

Cardozo, N., Allmendinger, R.W., Morgan, J.K., 2005. Influence of mechanical stratigraphy and initial stress state on the formation of two fault propagation folds. Journal of Structural Geology 27, 1954-1972.

Coleman, M.L., Raiswell, R., 1981. Carbon, oxygen and sulphur isotope variations in concretions from the Upper Lias of NE England. Geochimica et cosmochimica acta 45, 329-340.

Corbett, K., Friedman, M., Spang, J., 1987. Fracture development and mechanical stratigraphy of Austin Chalk, Texas. AAPG Bulletin 71, 17-28.

Cosgrove, J.W., 2001. Hydraulic fracturing during the formation and deformation of a basin: A factor in the dewatering of low-permeability sediments. AAPG Bulletin 85, 737-748.

Cundall, P.A., Strack, O.D.L., 1979. A discrete numerical model for granular assemblies. Geotechnique 29, 47-65.

Curtis, J.B., 2002. Fractured shale-gas systems. AAPG Bulletin 86, 1921-1938.

Dean, S.L., Morgan, J.K., Fournier, T., 2013. Geometries of frontal fold and thrust belts: Insights from discrete element simulations. Journal of Structural Geology 53, 43-53.

Finch, E., Gawthorpe, R., 2017. Growth and interaction of normal faults and fault network evolution in rifts: insights from three-dimensional discrete element modelling. Geological Society, London, Special Publications 439, https://doi.org/10.1144/SP439.23.

Finch, E., Hardy, S., Gawthorpe, R., 2003. Discrete element modelling of contractional fault-propagation folding above rigid basement fault blocks. Journal of Structural Geology 25, 515-528.

Finch, E., Hardy, S., Gawthorpe, R., 2004. Discrete-element modelling of extensional fault-propagation folding above rigid basement fault blocks. Basin Research 16, 467-488.

Gale, J.F.W., Holder, J., 2010. Natural fractures in some US shales and their importance for gas production. Geological Society, London, Petroleum Geology Conference series, 7, 1131-1140.

Gale, J.F.W., Laubach, S.E., Olson, J.E., Eichhubl, P., Fall, A., 2014. Natural fractures in shale: A review and new observationsNatural Fractures in Shale: A Review and New Observations. AAPG Bulletin 98, 2165-2216.

Guo, Y., Morgan, J.K., 2006. The frictional and micromechanical effects of grain comminution in fault gouge from distinct element simulations. Journal of Geophysical Research: Solid Earth 111, B12406, doi:10.1029/2005JB004049.

Guo, Y., Morgan, J.K., 2007. Fault gouge evolution and its dependence on normal stress and rock strength—Results of discrete element simulations: Gouge zone properties. Journal of Geophysical Research: Solid Earth 112, B10403, doi:10.1029/2006JB004524.

Hardy, S., 2011. Cover deformation above steep, basement normal faults: Insights from 2D discrete element modeling. Marine and Petroleum Geology 28, 966-972.

Hardy, S., 2013. Propagation of blind normal faults to the surface in basaltic sequences: Insights from 2D discrete element modelling. Marine and Petroleum Geology 48, 149-159.

Hardy, S., Finch, E., 2005. Discrete-element modelling of detachment folding. Basin Research 17, 507-520.

Hardy, S., Finch, E., 2006. Discrete element modelling of the influence of cover strength on basement-involved fault-propagation folding. Tectonophysics 415, 225-238.

Hardy, S., Finch, E., 2007. Mechanical stratigraphy and the transition from trishear to kink-band fault-propagation fold forms above blind basement thrust faults: a discrete-element study. Marine and Petroleum Geology 24, 75-90.

Hardy, S., McClay, K., Munoz, J.A., 2009. Deformation and fault activity in space and time in high-resolution numerical models of doubly vergent thrust wedges. Marine and Petroleum Geology 26, 232-248.

Holliday, D.W., 1970. The petrology of secondary gypsum rocks; a review. Journal of Sedimentary Research 40, 734-744.

Hooker, J.N., Cartwright, J., Stephenson, B., Silver, C.R.P., Dickson, A.J., Hsieh, Y.-T., 2017. Fluid evolution in fracturing black shales, Appalachian Basin. AAPG Bulletin 101, 1203-1238.

Hughes, A.N., Benesh, N.P., Shaw, J.H., 2014. Factors that control the development of fault-bend versus fault-propagation folds: Insights from mechanical models based on the discrete element method (DEM). Journal of Structural Geology 68, 121-141.

Imber, J., Tuckwell, G.W., Childs, C., Walsh, J.J., Manzocchi, T., Heath, A.E., Bonson, C.G., Strand, J., 2004. Three-dimensional distinct element modelling of relay growth and breaching along normal faults. Journal of Structural Geology 26, 1897-1911.

Irwin, H., Curtis, C., Coleman, M., 1977. Isotopic evidence for source of diagenetic carbonates formed during burial of organic-rich sediments. Nature 269, 209-213.

Kiriakoulakis, K., Marshall, J.D., Wolff, G.A., 2000. Biomarkers in a Lower Jurassic concretion from Dorset (UK). Journal of the Geological Society 157, 207-220.

Lash, G.G., Blood, D., 2004. Geochemical and textural evidence for early (shallow) diagenetic growth of stratigraphically confined carbonate concretions, Upper Devonian Rhinestreet black shale, western New York. Chemical Geology 206, 407-424.

Laubach, S.E., Olson, J.E., Gross, M.R., 2009. Mechanical and fracture stratigraphy. AAPG Bulletin 93, 1413-1426.

Liu, Y., Konietzky, H., 2018. Particle-Based Modeling of Pull-Apart Basin Development. Tectonics 37, 343-358.

Marshall, J.D., 1982. Isotopic composition of displacive fibrous calcite veins; reversals in pore-water composition trends during burial diagenesis. Journal of Sedimentary Research 52, 615-630.

Marshall, J.D., Pirrie, D., 2013. Carbonate concretions — explained. Geology Today 29, 53-62.

Meng, Q., Hooker, J., Cartwright, J., 2017a. Early overpressuring in organic-rich shales during burial: evidence from fibrous calcite veins in the Lower Jurassic Shales-with-Beef Member in the Wessex Basin, UK. Journal of the Geological Society 174, 869-882.

Meng, Q., Hooker, J., Cartwright, J., 2017b. Genesis of natural hydraulic fractures as an indicator of basin inversion. Journal of Structural Geology 102, 1-20.

Meng, Q., Hooker, J., Cartwright, J., 2018a. Lithological control on fracture cementation in the Keuper Marl (Triassic), north Somerset, UK. Geological Magazine 155, 1761-1775.

Meng, Q., Hooker, J., Cartwright, J., 2018b. Quantifying vein attributes in massive mudstones (Triassic, SW England): Implications for progressive evolution of opening-mode fracture networks. Marine and Petroleum Geology 98, 523-532.

Morgan, J.K., 2015. Effects of cohesion on the structural and mechanical evolution of fold and thrust belts and contractional wedges: Discrete element simulations. Journal of Geophysical Research: Solid Earth 120, 3870-3896.

Morgan, J.K., Bangs, N.L., 2017. Recognizing seamount-forearc collisions at accretionary margins: Insights from discrete numerical simulations. Geology 45, 635-638.

Mozley, P.S., Burns, S.J., 1993. Oxygen and carbon isotopic composition of marine carbonate concretions; an overview. Journal of Sedimentary Research 63, 73-83.

Mozley, P.S., Wersin, P., 1992. Isotopic composition of siderite as an indicator of depositional environment. Geology 20, 817-820.

Naylor, M., Sinclair, H.D., Willett, S., Cowie, P.A., 2005. A discrete element model for orogenesis and accretionary wedge growth. Journal of Geophysical Research: Solid Earth 110, B12403, doi:10.1029/2003JB002940.

Nichols, G., 2009. Sedimentology and stratigraphy. John Wiley & Sons.

Pichel, L.M., Finch, E., Huuse, M., Redfern, J., 2017. The influence of shortening and sedimentation on rejuvenation of salt diapirs: A new Discrete-Element Modelling approach. Journal of Structural Geology 104, 61-79.

Potter, P.E., Maynard, J.B., Depetris, P.J., 2005. Mud and mudstones: Introduction and overview. Springer Science & Business Media.

Raiswell, R., Fisher, Q.J., 2000. Mudrock-hosted carbonate concretions: a review of growth mechanisms and their influence on chemical and isotopic composition. Journal of the Geological Society 157, 239-251.

Rodrigues, N., Cobbold, P.R., Loseth, H., Ruffet, G., 2009. Widespread bedding-parallel veins of fibrous calcite ('beef') in a mature source rock (Vaca Muerta Fm, Neuquén Basin, Argentina): evidence for overpressure and horizontal compression. Journal of the Geological Society 166, 695-709.

Saltzer, S.D., 1992. Boundary conditions in sandbox models of crustal extension: an analysis using distinct elements. Tectonophysics 215, 349-362.

Schöpfer, M.P.J., Arslan, A., Walsh, J.J., Childs, C., 2011. Reconciliation of contrasting theories for fracture spacing in layered rocks. Journal of Structural Geology 33, 551-565.

Schöpfer, M.P.J., Childs, C., Walsh, J.J., 2006. Localisation of normal faults in multilayer sequences. Journal of Structural Geology 28, 816-833.

Schöpfer, M.P.J., Childs, C., Walsh, J.J., 2007. Two-dimensional distinct element modeling of the structure and growth of normal faults in multilayer sequences: 1. Model calibration, boundary conditions, and selected results. Journal of Geophysical Research: Solid Earth 112, B10401, doi:10.1029/2006JB004902.

Schöpfer, M.P.J., Childs, C., Walsh, J.J., Manzocchi, T., 2016. Evolution of the internal structure of fault zones in three-dimensional numerical models of normal faults. Tectonophysics 666, 158-163.

Schoepfer, M.P.J., Childs, C., Manzocchi, T., Walsh, J.J., Nicol, A., Grasemann, B., 2017. The emergence of asymmetric normal fault systems under symmetric boundary conditions. Journal of Structural Geology 104, 159-171.

Smart, K.J., Wyrick, D.Y., Ferrill, D.A., 2011. Discrete element modeling of Martian pit crater formation in response to extensional fracturing and dilational normal faulting. Journal of Geophysical Research: Planets 116, E04005, doi:10.1029/2010JE003742.

Spence, G.H., Finch, E., 2014. Influences of nodular chert rhythmites on natural fracture networks in carbonates: an outcrop and two-dimensional discrete element modelling study. Geological Society, London, Special Publications 374, 211-249.

Strayer, L.M., Suppe, J., 2002. Out-of-plane motion of a thrust sheet during along-strike propagation of a thrust ramp: a distinct-element approach. Journal of Structural Geology 24, 637-650.

St. John, J., 2015a. https://commons.wikimedia.org/wiki/File:Normal_fault_in_the_Lowellville_Shale_(Pottsville_Group,_Lower_Pennsylvanian;_Beach_City_Dam_outcrop,_northeastern_Ohio,_USA)_2_(25190907573).jpg (accessed 31 October 2015), CC BY 2.0

St. John, J., 2015b. <https://commons.wikimedia.org/wiki/File:Fault_in_the_Lowellville_Shale_(Pottsville_Group,_Lower_Pennsylvanian;_Beach_City_Dam_outcrop,_northeastern_Ohio,_USA)_1_(25696458192).jpg> (accessed 31 October 2015), CC BY 2.0

Tucker, M.E., 2009. Sedimentary petrology: an introduction to the origin of sedimentary rocks. John Wiley & Sons.

Vidal-Royo, O., Hardy, S., Muñoz, J.A., 2011. The roles of complex mechanical stratigraphy and syn-kinematic sedimentation in fold development: insights from discrete-element modelling and application to the Pico del Águila anticline (External Sierras, Southern Pyrenees). Geological Society, London, Special Publications 349, 45-60.

Virgo, S., Abe, S., Urai, J.L., 2013. Extension fracture propagation in rocks with veins: Insight into the crack-seal process using Discrete Element Method modeling. Journal of Geophysical Research: Solid Earth 118, 5236-5251.

Virgo, S., Abe, S., Urai, J.L., 2014. The evolution of crack seal vein and fracture networks in an evolving stress field: Insights from Discrete Element Models of fracture sealing. Journal of Geophysical Research: Solid Earth 119, 8708-8727.

Virgo, S., Abe, S., Urai, J.L., 2016. The influence of loading conditions on fracture initiation, propagation, and interaction in rocks with veins: Results from a comparative Discrete Element Method study. Journal of Geophysical Research: Solid Earth 121, 1730-1738.

Wolff, G.A., Rukin, N., Marshall, J.D., 1992. Geochemistry of an early diagenetic concretion from the Birchi Bed (L. Lias, W. Dorset, UK). Organic Geochemistry 19, 431-444.

Yamada, Y., Matsuoka, T., 2005. Digital sandbox modeling using distinct element method: Applications to fault tectonics. AAPG Memoir 85, 107-123.

Young, B.W., Chan, M.A., 2017. Gypsum veins in Triassic Moenkopi mudrocks of southern Utah: Analogs to calcium sulfate veins on Mars. Journal of Geophysical Research: Planets 122, 150-171.

Figure captions

Fig. 1. Schematic illustration showing the model design, boundary conditions and particle interactions.

Fig. 2. Result of model I showing sequential generation of fractures. T1 to T6 represent timestep of $5x10^4$, $8x10^4$, $1x10^5$, $1.3x10^5$, $1.6x10^5$ and $2.0x10^5$ respectively. See text for description.

Fig. 3. Contour of displacement field of model I. See text for description.

Fig. 4. Contact force chains of model I with soft nodules (gray). See text for description.

Fig. 5. Plot of fracture number versus timestep for model I with soft nodules.

Fig. 6. Result of model II showing sequential generation of fractures. T1 to T6 represent timestep of $1.5x10^5$, $2.0\ x10^5$, $2.5\ x10^5$, $3.0\ x10^5$, $3.5\ x10^5$ and $4.0\ x10^5$ respectively. The enlarged box shows the opening void between nodule 3 and its enclosing rock. See text for description.

Fig. 7. Contour of displacement field of model II. See text for description.

Fig. 8. Contact force chains of model II with stiff nodules (gray). See text for description.

Fig. 9. Plot of fracture number versus timestep for model II with stiff nodules.

Fig. 10. Field photographs showing gypsum nodules and veins in the red Triassic marls of the Bristol Channel Basin, UK. (a) Horizontal bridging veins (arrows) link neighboring nodules. Note that the veins are rooted in nodules and exhibit tapering tips. (b) Horizontal (green) and sub-vertical (yellow) bridging veins are developed within three nodular horizons.

Fig. 11. Field photographs showing gray limestone nodules and faults in black shales of the Pottsville Group, northeastern Ohio, USA. Modified from St. John (2015a, b). (a) A fault transects the outcrop of black shales. The fault cross-cuts the upper surface of nodule *a* and the lower surface of nodule *b*. (b) A fault F1 is developed along the interface between shale and a lenticular nodule. Faults and fractures are highlighted by dashed lines. The enlarged box shows the fault trace of F1.

Table.1 Parameters for the discrete element models.

Parameter	Rock matrix	Soft nodule	Stiff nodule
Particle number	68,433	1189 x 6	1189 x 6
Particle radii (m)	0.01-0.012	0.01-0.012	0.01-0.012
Density (kg/m^3)	2600	2600	2600
Porosity (%)	10	10	10
Particle normal stiffness k_n (N/m)	1e8	1e7	1e9
Particle shear stiffness k_s (N/m)	5e7	5e6	5e8
Bond normal stiffness $\overline{k_n}$ (N/m)	1e8	1e7	1e9
Bond shear stiffness $\overline{k_s}$ (N/m)	5e7	5e6	5e8
Bond cohesion $\overline{\sigma_c}$ (N)	5e4	5e3	5e5
Bond tensile strength $\bar{c}$ (N)	2e5	2e4	2e6
Young's modulus E (MPa)	50	5	500
Friction coefficient μ	0.25	0.25	0.25

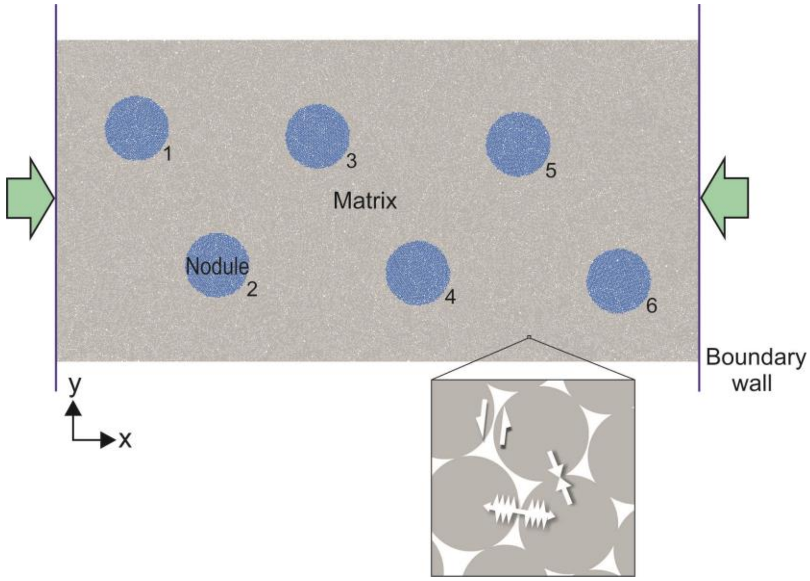

Fig. 1

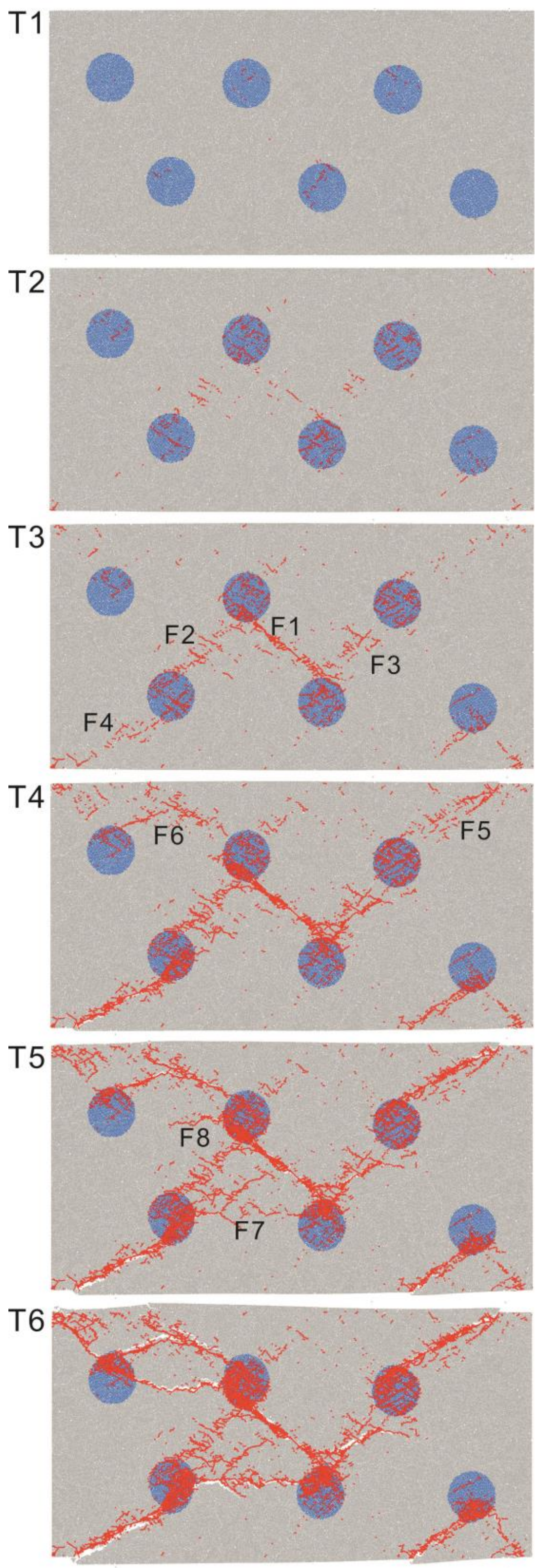

Fig. 2

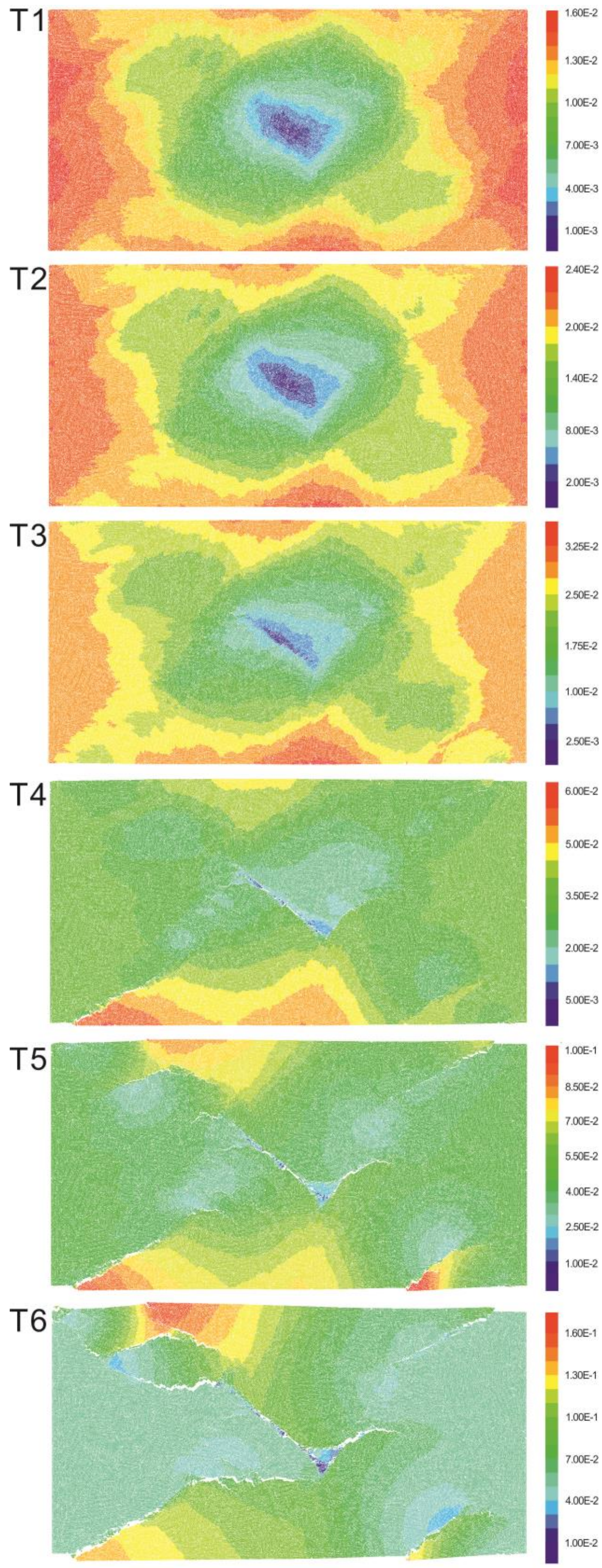
T1
1.60E-2
1.30E-2
1.00E-2
7.00E-3
4.00E-3
1.00E-3
T2
2.40E-2
2.00E-2
1.40E-2
8.00E-3
2.00E-3
T3
3.25E-2
2.50E-2
1.75E-2
1.00E-2
2.50E-3
T4
6.00E-2
5.00E-2
3.50E-2
2.00E-2
5.00E-3
T5
1.00E-1
8.50E-2
7.00E-2
5.50E-2
4.00E-2
2.50E-2
1.00E-2
T6
1.60E-1
1.30E-1
1.00E-1
7.00E-2
4.00E-2
1.00E-2

Fig. 3

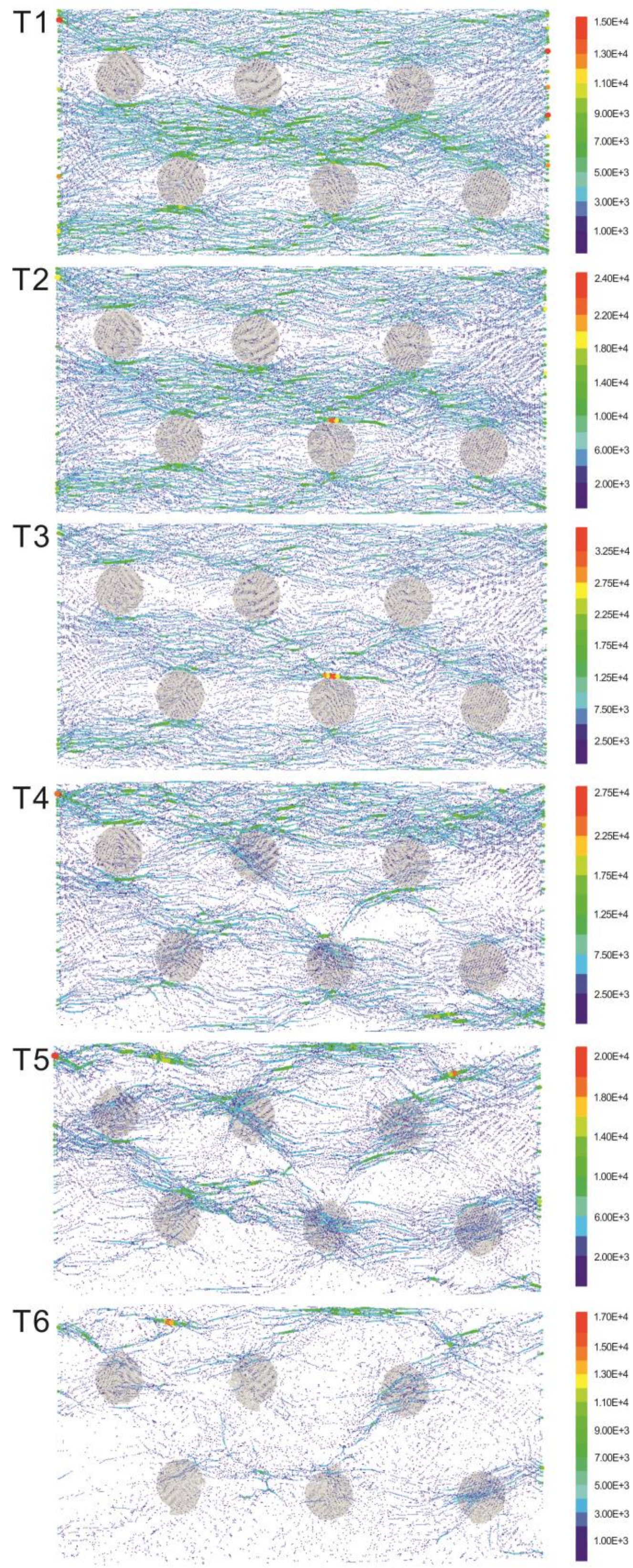
T1
1.50E+4
1.30E+4
1.10E+4
9.00E+3
7.00E+3
5.00E+3
3.00E+3
1.00E+3
T2
2.40E+4
2.20E+4
1.80E+4
1.40E+4
1.00E+4
6.00E+3
2.00E+3
T3
3.25E+4
2.75E+4
2.25E+4
1.75E+4
1.25E+4
7.50E+3
2.50E+3
T4
2.75E+4
2.25E+4
1.75E+4
1.25E+4
7.50E+3
2.50E+3
T5
2.00E+4
1.80E+4
1.40E+4
1.00E+4
6.00E+3
2.00E+3
T6
1.70E+4
1.50E+4
1.30E+4
1.10E+4
9.00E+3
7.00E+3
5.00E+3
3.00E+3
1.00E+3

Fig. 4

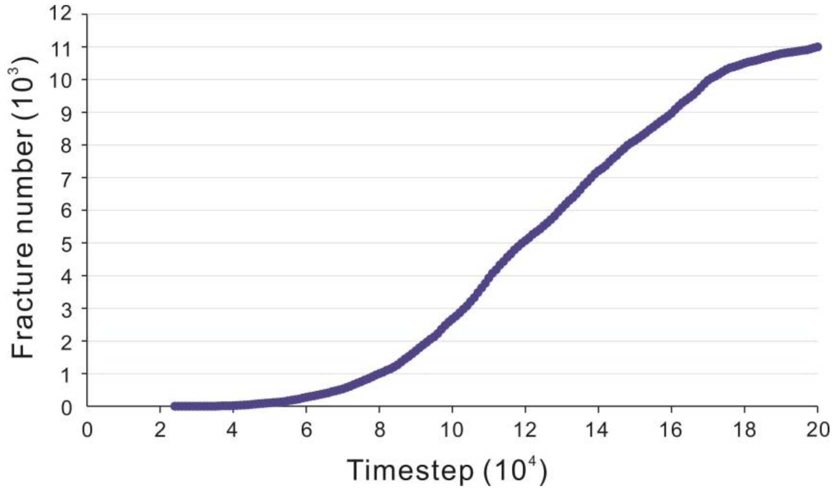
Fracture number (10^3)
0
1
2
3
4
5
6
7
8
9
10
11
12
0
2
4
6
8
10
12
14
16
18
20
Timestep (10^4)

Fig. 5

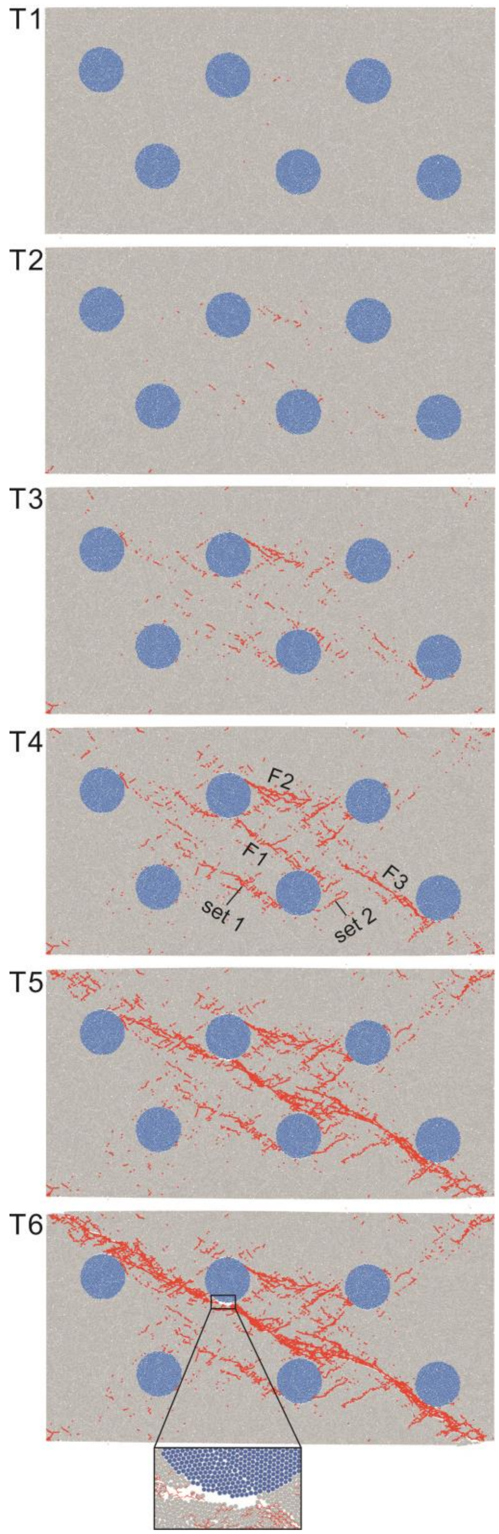

Fig. 6

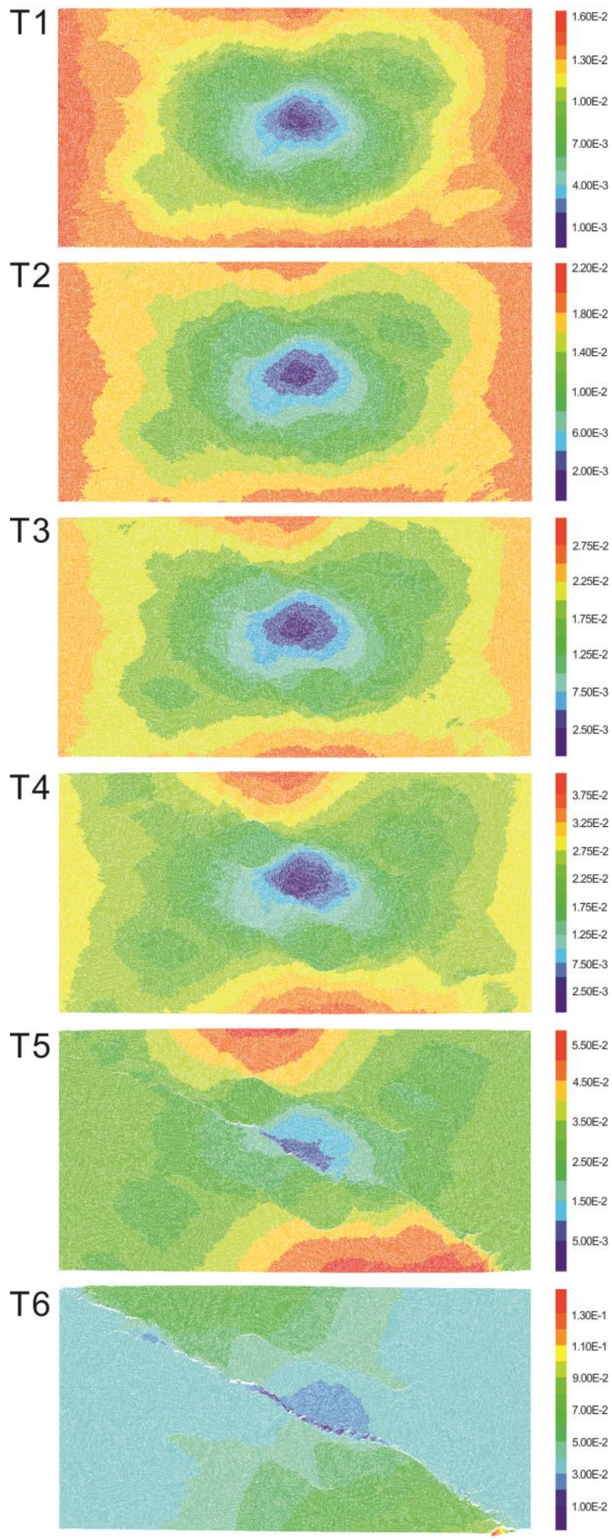
T1
1.60E-2
1.30E-2
1.00E-2
7.00E-3
4.00E-3
1.00E-3
T2
2.20E-2
1.80E-2
1.40E-2
1.00E-2
6.00E-3
2.00E-3
T3
2.75E-2
2.25E-2
1.75E-2
1.25E-2
7.50E-3
2.50E-3
T4
3.75E-2
3.25E-2
2.75E-2
2.25E-2
1.75E-2
1.25E-2
7.50E-3
2.50E-3
T5
5.50E-2
4.50E-2
3.50E-2
2.50E-2
1.50E-2
5.00E-3
T6
1.30E-1
1.10E-1
9.00E-2
7.00E-2
5.00E-2
3.00E-2
1.00E-2

Fig. 7

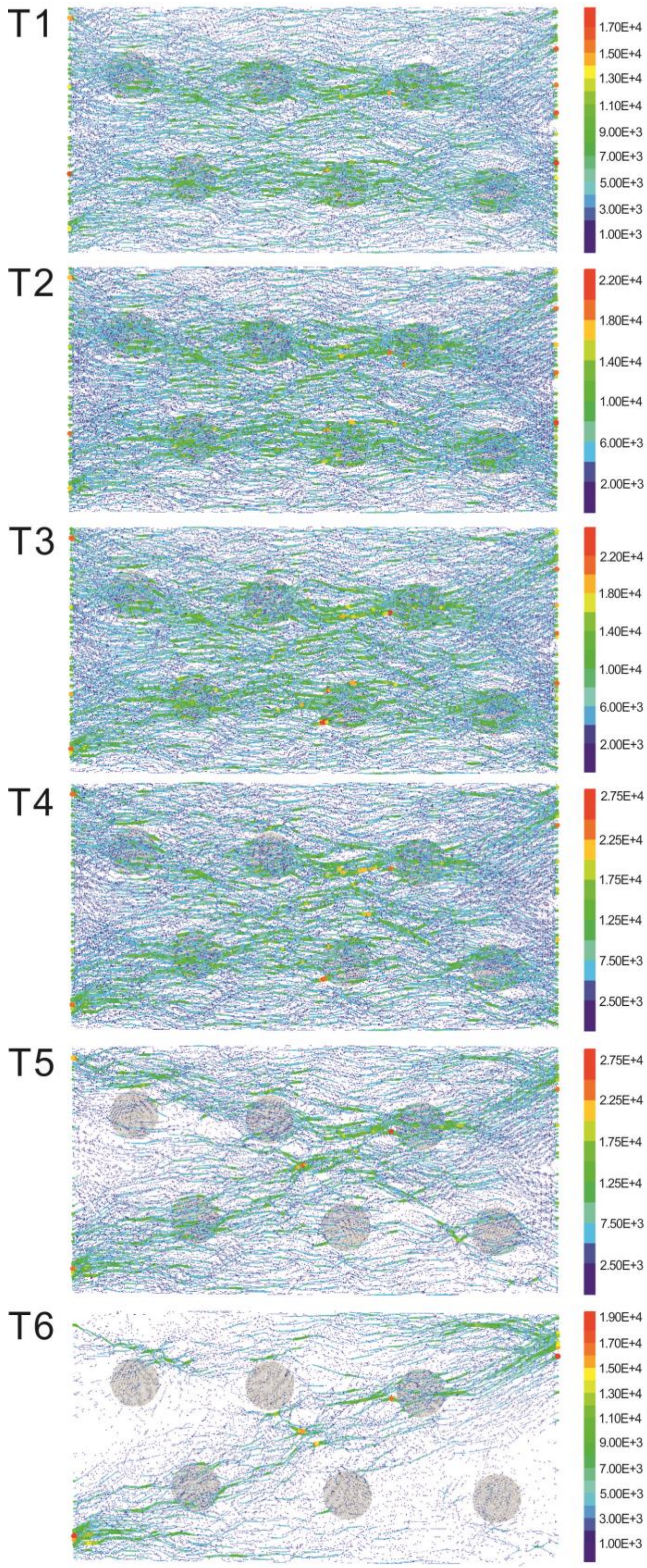
T1
1.70E+4
1.50E+4
1.30E+4
1.10E+4
9.00E+3
7.00E+3
5.00E+3
3.00E+3
1.00E+3
T2
2.20E+4
1.80E+4
1.40E+4
1.00E+4
6.00E+3
2.00E+3
T3
2.20E+4
1.80E+4
1.40E+4
1.00E+4
6.00E+3
2.00E+3
T4
2.75E+4
2.25E+4
1.75E+4
1.25E+4
7.50E+3
2.50E+3
T5
2.75E+4
2.25E+4
1.75E+4
1.25E+4
7.50E+3
2.50E+3
T6
1.90E+4
1.70E+4
1.50E+4
1.30E+4
1.10E+4
9.00E+3
7.00E+3
5.00E+3
3.00E+3
1.00E+3

Fig. 8

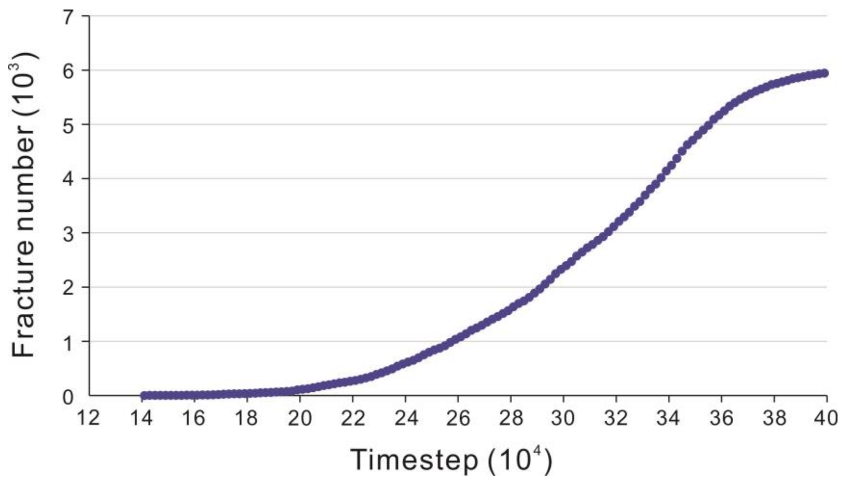
Fracture number (10^3)
0
1
2
3
4
5
6
7
12
14
16
18
20
22
24
26
28
30
32
34
36
38
40
Timestep (10^4)

Fig. 9

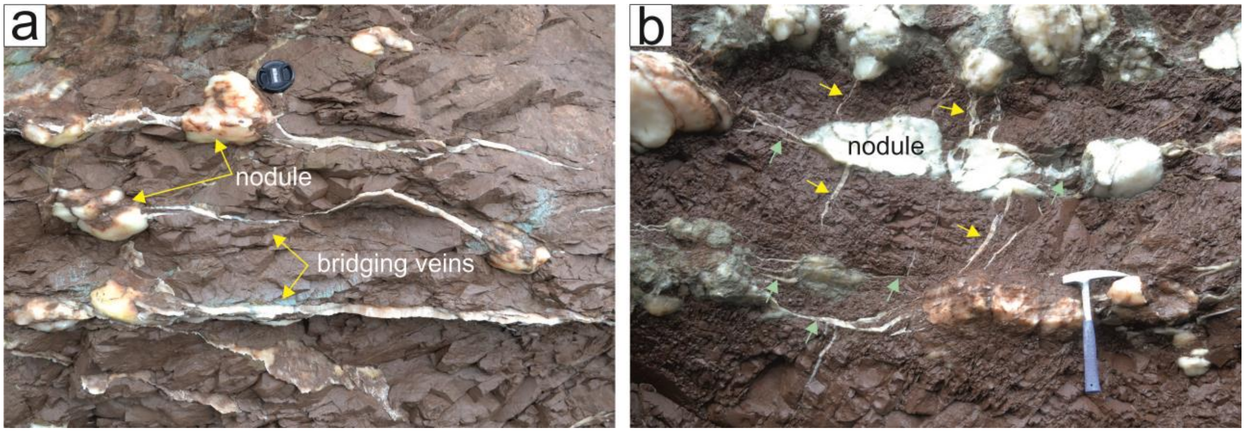

Fig. 10

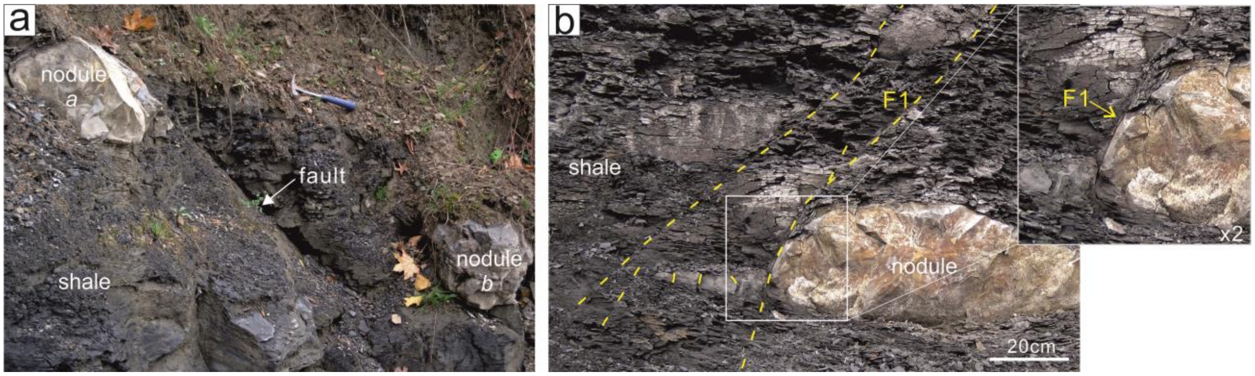

Fig. 11